Microsc. Microanal. Page 1 of 7
doi:10.1017/S1431927613001475

Microscopy AND Microanalysis

Chromatic Aberration-Corrected Tilt Series Transmission Electron Microscopy of Nanoparticles in a Whole Mount Macrophage Cell

Jean-Pierre Baudoin,[1] Joerg R. Jinschek,[2] Chris B. Boothroyd,[3] Rafal E. Dunin-Borkowski,[3] and Niels de Jonge[1,4,*]

[1]*Department of Molecular Physiology and Biophysics, Vanderbilt University School of Medicine, Nashville, TN 37232-0615, USA*
[2]*FEI Company Europe, 5600 KA Eindhoven, The Netherlands*
[3]*Forschungszentrum Jülich, Ernst Ruska-Centre for Microscopy and Spectroscopy with Electrons (ER-C) and Peter Grünberg Institute (PGI), D-52425 Jülich, Germany*
[4]*INM-Leibniz Institute for New Materials, D-66123 Saarbrücken, Germany*

Abstract: Transmission electron microscopy (TEM) in combination with electron tomography is widely used to obtain nanometer scale three-dimensional (3D) structural information about biological samples. However, studies of whole eukaryotic cells are limited in resolution and/or contrast on account of the effect of chromatic aberration of the TEM objective lens on electrons that have been scattered inelastically in the specimen. As a result, 3D information is usually obtained from sections and not from whole cells. Here, we use chromatic aberration-corrected TEM to record bright-field TEM images of nanoparticles in a whole mount macrophage cell. Tilt series of images are used to generate electron tomograms, which are analyzed to assess the spatial resolution that can be achieved for different vertical positions in the specimen. The uptake of gold nanoparticles coated with low-density lipoprotein (LDL) is studied. The LDL is found to assemble in clusters. The clusters contain nanoparticles taken up on different days, which are joined without mixing their nanoparticle cargo.

Key words: whole eukaryotic cell, low-density lipoprotein, specific labels, gold nanoparticles, tomography, three dimensions, spatial resolution, thick sample

Introduction

Transmission electron microscopy (TEM) is widely used to obtain nanometer scale information about intracellular components (Pierson et al., 2009; Gan & Jensen, 2012; Kourkoutis et al., 2012). However, a fundamental limitation of bright-field TEM is the need for the specimen to be thinner than ~0.5 μm, in particular when recording a tomographic tilt series of images to obtain three-dimensional (3D) information (Hoenger & McIntosh, 2009). As eukaryotic cells are at least several micrometers thick, studies of ultrastructure are therefore carried out primarily at cell edges (Medalia et al., 2002) or using thin sections. This restriction on specimen thickness is a consequence of (1) the angular scattering of electrons in a thick specimen, (2) different parts of the specimen being at different defocus values, and (3) the image blurring that results from electrons that suffered different energy losses in the specimen leading to different focal lengths due to the chromatic aberration of the objective lens (Reimer & Gentsch, 1975; Reimer & Kohl, 2008). Although the spatial resolution and depth of field of a bright-field TEM image of a thick specimen can in principle be optimized by selecting an optimal objective aperture size, using energy filtering, and selecting an objective lens excitation that results in electrons with the most probable energy loss in the specimen being imaged in focus (Reimer & Ross-Messemer, 1987), this approach results in an increased electron dose and cannot be applied effectively if the specimen thickness varies substantially across the field of view (Koster et al., 1997). Another approach is to use scanning transmission electron microscopy (Yakushevska et al., 2007; Aoyama et al., 2008; Engel, 2009; Hohmann-Marriott et al., 2009; Hohn et al., 2011), which has been applied to locate the positions of proteins labeled with nanoparticles in micrometer-thick samples (Sousa et al., 2007; de Jonge et al., 2010*a*; Dukes et al., 2011). The 3D structure of cells can also be studied via a serial sectioning process using scanning electron microscopy (Heymann et al., 2006) or with X-ray tomography (Larabell & Nugent, 2010), albeit at a lower resolution than achievable with tilt series TEM.

A recent development in electron microscopy is the introduction of a corrector for chromatic aberration of the TEM objective lens (Haider et al., 2009; Kabius et al., 2009; Leary & Brydson, 2011). As inelastically scattered electrons typically lose energy without changing their direction significantly, it is expected that the use of chromatic aberration correction will allow a much larger fraction of the incident electrons to be used to record high spatial resolution images than by using energy filtering. It is therefore of great interest to assess the spatial resolution that can be achieved in images of whole cells recorded using chromatic aberration-corrected TEM.

Here, we describe first experiments involving the application of a newly developed chromatic aberration-corrected

Received January 11, 2013; accepted March 25, 2013
*Corresponding author. E-mail: niels.de.jonge@inm-gmbh.de

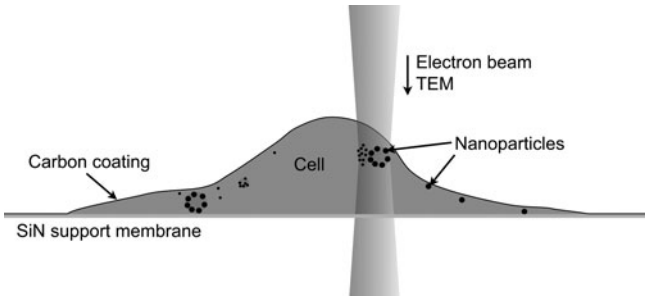

Figure 1. Schematic diagram depicting transmission electron microscopy (TEM) of a whole mount cell. The cell was grown on a silicon nitride (SiN) support membrane, fixed and critical point dried. A thin coating of carbon increased the stability of the cell under electron beam irradiation. Two different sizes of gold nanoparticles were used as specific protein labels to study the uptake processes of low-density lipoprotein.

TEM to study whole mount macrophage cells. As an example of a biological experiment that can be addressed with whole cell imaging, we investigated the uptake of gold nanoparticles coated with low-density lipoprotein (LDL) to study lipoprotein uptake and trafficking (Jerome & Yancey, 2003; Luzio et al., 2007; Ikonen, 2008). Cells were grown on a support membrane, incubated with the nanoparticles, prepared for TEM, and imaged as shown schematically in Figure 1. We generated tomograms from tilt series of chromatic aberration-corrected TEM images in order to study the 3D positions of the plasma membrane ruffles and gold nanoparticles. The spatial resolution was measured for different depths in the specimen.

Materials and Methods

Sample Preparation

Macrophages derived from monocytes (THP-1 cells, American Type Culture Collection) were grown directly onto electron transparent silicon nitride TEM support windows (Protochips Inc., Raleigh, NC, USA) (Dukes et al., 2011) in phorbol-12-myristate-13-acetate-supplemented medium (Jerome et al., 2008). Native LDL was conjugated to gold nanoparticles (Jerome et al., 2008) that had been prepared by reducing gold chloride (Frens, 1973). The diameters of the nanoparticles were measured to be 16 ± 3 or 7 ± 1 nm from line scans measured from bright-field TEM images. Live cells were incubated with 16-nm LDL-gold on the first day and 7-nm LDL-gold on the second day. The incubation took place at 37°C in 1% fetal bovine serum medium with an equivalent concentration of 8 μg/mL LDL. In order to prepare samples for electron microscopy, the cells were rinsed with phosphate-buffered saline, fixed with glutaraldehyde 2.5% in 0.1 molar sodium cacodylate buffer/0.05% $CaCl_2$, postfixed with an ultra-low concentration (0.001%) of osmium tetroxide, gradually dehydrated with ethanol and critical point dried with liquid carbon dioxide (Dukes et al., 2011). Critical point drying preserves the volume of the cell and fine structures such as membrane ruffles, but may lead to 20–40% flattening of the cells (Gusnard & Kirschner, 1977). Approximately 20 nm of carbon was evaporated onto the microchips to improve their resistance to electron beam damage (Dukes et al., 2011). The carbon was applied in an electron beam evaporator of local design with a base pressure of 5×10^{-7} torr. The evaporation time was ~45 min.

TEM

Bright-field TEM images were recorded at 300 kV using an FEI Titan 80-300 "PICO" electron microscope (PICO project, ER-C, Jülich, Germany), which is equipped with an objective lens corrector for both chromatic and spherical aberration. In the present study, spherical aberration is insignificant when compared to other sources of degradation in image resolution. Tilt series of 2,048 × 2,048 pixel bright-field TEM images were acquired at specimen tilt angles of −40° to 34° in 2° steps using an objective aperture of semiangle 10 mrad, and a 1 s acquisition time. Higher specimen tilt angles could not be reached because of shadowing by the windows in the silicon microchip used to support the silicon nitride membrane on which the cells were grown.

Image Processing

Although the range of specimen tilt angles that could be accessed experimentally was limited, information about the heights of cell features could be measured from tomograms reconstructed from each tilt series. The tomograms were generated by applying a weighted back projection algorithm using the IMOD software package (University of Colorado, Boulder, CO, USA) (Kremer et al., 1996) on a MacPro computer equipped with 2 × 2.4 GHz quad-core Intel Xeon processors and 16 Gb RAM.

Four tomograms were reconstructed: (1) A tilt series of a cellular domain was recorded at a magnification of 3,300× using a pixel size of 4.53 nm (Fig. 2a; Supplementary Movie 1) and used to generate a 9,277 × 9,277 × 4,194-nm^3 tomogram (Fig. 2b; Supplementary Movie 2), as well as a 3D model of the plasma membrane and clusters of nanoparticles (Fig. 2c; Supplementary Movie 3). (2) A tilt series of a perinuclear domain was recorded at a magnification of 9,800× using a pixel size of 1.46 nm (Fig. 3b) and used to generate a 2,990 × 2,990 × 2,091-nm^3 tomogram (Fig. 3c, Supplementary Movie 4). (3) A tilt series of the region boxed in Figure 4a was recorded at a magnification of 17,000× using a pixel size of 0.88 nm and used to generate a 1,802 × 1,802 × 883-nm^3 tomogram (data not shown). (4) A tilt series of the region boxed in Figure 4a (Fig. 4b) was recorded at a magnification of 34,000× using a pixel size of 0.44 nm, used to generate a 396 × 396 × 688-nm^3 tomogram (Supplementary Movie 5), and analyzed to determine the 3D positions of individual nanoparticles (Fig. 4c; Supplementary Movie 5). The specimen thickness was determined by measuring the distance between the lowest nanoparticle appearing in each tomogram, which coincided with the appearance of the intracellular space, and the top of the membrane ruffles.

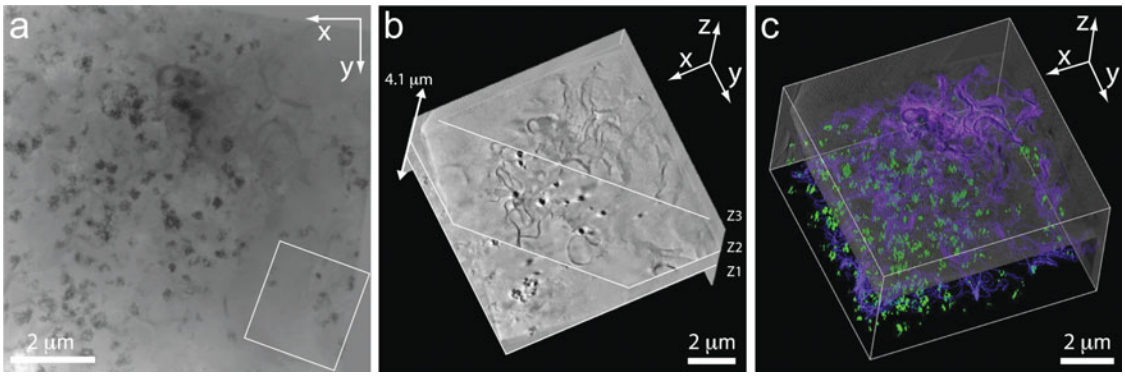

Figure 2. Chromatic aberration-corrected transmission electron microscopy (TEM) tilt series of a whole mount macrophage cell. The acceleration voltage was 300 kV, the magnification was 3,300×, the pixel size was 4.53 nm, the objective aperture semiangle was 10 mrad, and the acquisition time was 1 s. The tilt series ranged from −40° to 34° in 2° steps. **a:** TEM image recorded at 0° tilt showing low-density lipoprotein-coated gold nanoparticles assembled in clusters in the cell. The boxed region was used for electron energy loss spectroscopy. **b:** Three-dimensional (3D) reconstruction generated from the tilt series corresponding to (**a**). The dimensions of the tomogram were 9,277 × 9,277 × 4,194 nm^3 along *x*, *y*, and *z*, respectively. Three cutout slices 154 nm thick along the height of the tomogram are shown: Z1 at +199 nm, Z2 at +1,957 nm, and Z3 at +2,709 nm. **c:** 3D model of the tomogram depicted in (**b**). Nanoparticle clusters are colored green, whereas plasma membrane ruffles are colored blue. The clusters of gold nanoparticles were distributed over 2.53 μm in vertical direction, from the bottom-most to the top-most nanoparticle.

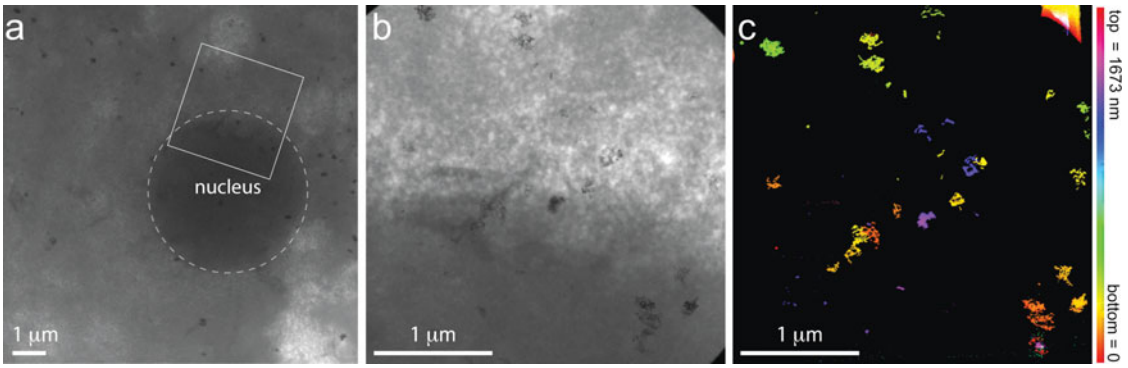

Figure 3. Chromatic aberration-corrected transmission electron microscopy (TEM) tilt series of a whole mount macrophage cell perinuclear region. **a:** Single TEM image at 2,550× magnification (pixel size of 5.45 nm) showing a cellular region comprising a nucleus (dashed circle). **b:** TEM image at 0° tilt selected from a tilt series, showing the clusters of gold nanoparticles in the 2.10-μm-thick boxed region in (**a**). The magnification was 9,800× (pixel size of 1.46 nm). **c:** Maximal intensity projection of the tomogram resulting from tilt series acquisitions in (**b**). The clusters of gold nanoparticles were distributed over 1.67 μm in the vertical direction, from the bottom-most to the top-most nanoparticle.

Supplementary Material

To view supplementary material (Supplementary Movies 1–5) for this article, please visit http://dx.doi.org/10.1017/S1431927613001475.

In order to visualize the plasma membrane and the clusters of nanoparticles in the tomogram shown in Figure 2b, its size was reduced from 2,048 × 2,048 × 1,010 to 512 × 512 × 505 pixels. A 3D model of the plasma membrane was then obtained by drawing contours around the membrane ruffles in horizontal sections that were spaced by 54 nm along *z*. The 3D model of the clusters of nanoparticles was obtained from an isosurface based on an intensity threshold. The 3D models of the plasma membrane and the clusters of nanoparticles were then combined for simultaneous visualization (Fig. 2c, Supplementary Movie 3). The model was made isotropic (voxels with the same length in all dimensions) in the three dimensions for correct visualization.

To determine the vertical positions of the individual nanoparticles in the tomogram derived from the tilt series shown in Figure 4b (Supplementary Movie 5), we made use of known information about their shapes to determine their positions with better precision than the vertical resolution of the tomogram (van Aert et al., 2011). The vertical positions of the nanoparticles were measured from their maximal intensities in the tomogram. This procedure was possible for nanoparticles spaced sufficiently far apart that they could be distinguished as individual nanoparticles. Their horizontal locations and diameters were determined from the corresponding *xy* slice. Finally, spheres of corresponding diameter were positioned at the measured 3D locations (Fig. 4c; Supplementary Movie 5).

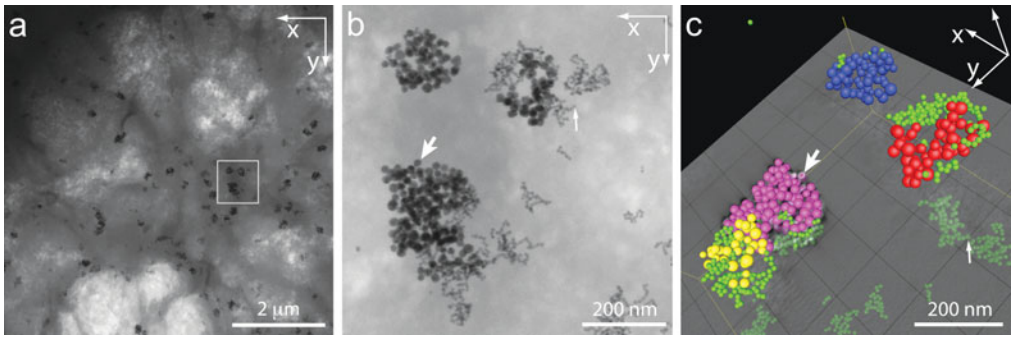

Figure 4. Three-dimensional (3D) reconstruction of gold nanoparticle clusters from chromatic aberration-corrected transmission electron microscopy (TEM) tilt series. **a:** Overview image at 4,300× magnification (pixel size 3.39 nm). **b:** TEM image at 0° tilt showing clusters containing different sizes of gold nanoparticles in the region boxed in (**a**). The magnification was 34,000× with a pixel size of 0.44 nm. For this region, a thickness of 0.88 μm was calculated in a tomogram derived from a second tilt series acquired in the same region but at a lower magnification of 17,000×. **c:** 3D reconstruction of the individual nanoparticles in the cellular region centered on the cluster shown in (**b**) (magenta). The dimensions of the tomogram were 396 × 396 × 688 nm^3 in *x*, *y*, and *z*, respectively. The 7-nm-diameter nanoparticles are shown in green; 16-nm-diameter nanoparticles are shown in magenta, yellow, red, and blue. The arrows point toward the same nanoparticles in both (**b**) and (**c**).

Results and Discussion

Preparation of Whole Mount Cellular Samples and Incubation with LDL-Gold

Whole mount cellular samples were prepared from macrophage cells. The whole mount technique provides a practical way to study a whole cell, as it is much more difficult to include the cellular volume in a conventional thin section. The cells were grown directly onto silicon nitride support membranes. Electron beam irradiation-resistant whole mount cellular samples were prepared by fixation, staining with a low concentration of osmium tetroxide, critical-point drying, and carbon coating (Dukes et al., 2011). Additional staining (e.g., with lead) was avoided to be able to image through the entire cell. Instead of studying the ultrastructure of organelles within the cellular volume, we focused on the visualization of nanoparticles coated with LDL and their uptake.

An important problem in biology that is not yet fully understood is the deleterious transformation of macrophages into foam cells during atherosclerosis (Moore & Tabas, 2011). It is known that LDL-derived cholesterol accumulates in macrophages, which are progressively converted into foam cells (Jerome & Yancey, 2003). However, it is not clear how this accumulation occurs, that is, what the fate of the LDL is after its intracellular trafficking (Jerome & Yancey, 2003; Luzio et al., 2007). Proteins that have been taken up by cells are classically internalized by endosomes (endocytosis) and ultimately delivered to lysosomes, the cellular compartments that degrade proteins (Luzio et al., 2007). After being taken up by endocytosis, LDL is degraded slowly and finally digested in lysosomes. As they cannot be degraded, gold nanoparticles can be used as fiducial markers to follow the fate of LDL along its trafficking compartments in macrophages (Jerome et al., 2008). TEM studies of thin sections demonstrated that the LDL-coated gold nanoparticles ended up in lysosomes (Yancey et al., 2002). Here, we assess whether LDL that has been taken up by a cell at a certain time ends up in trafficking compartments filled with LDL that were previously internalized, or whether new compartments are formed. For this purpose, macrophage cells were incubated with LDL-gold nanoparticles of diameter 16 ± 3 nm for 1 day, followed by loading with nanoparticles of diameter 7 ± 1 nm for a further day. The 3D organization of the gold nanoparticles was determined from tilt series of chromatic aberration-corrected bright-field TEM images.

Chromatic Aberration-Corrected TEM Tilt Series

Tilt series of chromatic aberration-corrected bright-field TEM images were recorded from different cellular regions at different magnifications. Figure 2a shows an image of LDL-gold nanoparticle clusters acquired at 0° specimen tilt (the entire tilt series can be seen in Supplementary Movie 1). Clusters of nanoparticles are visible in the image, in addition to cellular features consisting of plasma membrane ruffles that delineate the upper cell boundary. A tomographic reconstruction (Fig. 2b; Supplementary Movie 2) was performed to establish the 3D positions of the clusters in the cell. In the thickest region, in which the highest plasma membrane ruffles reach a height of 4.1 μm, the nanoparticle clusters are measured to be distributed in a 2.53-μm-thick intracellular space below the membrane ruffles. Figure 2b shows three horizontal (*xy*) slices, which have been extracted from the tomogram and show plasma membrane ruffles at the top of the cell. The ruffles are also present at lower positions, toward the bottom left corner of Figure 2b and Supplementary Movie 2, indicating that the cell body is thinner there. An intracellular space filled with clusters of LDL-gold nanoparticles is visible below the membrane ruffles. Although a 3D visualization of the tomogram depicted in Figure 2b (Fig. 2c; Supplementary Movie 3) contains artifacts resulting from the limited tilt range of ±37°, such as elongation in the vertical direction, the clusters and the membrane ruffles can be identified. Individual nanoparticles cannot be resolved at this magnification.

Table 1. Measurement of Spatial Resolution from Two Tomograms, Which Correspond First to Figure 3b and Supplementary Movie 4 and Second to Figure 4b and Supplementary Movie 5.*

			xy plane		*xz* plane
Tomogram	T (μm)	z (nm)	$r_{25–75}$ (nm)	FWHM (nm)	FWHM (nm)
Figure 3b	2.09	145 ± 25 ($n = 10$)	2.5 ± 0.4	7.0 ± 1.0	16.0 ± 5.5
		546 ± 63 ($n = 10$)	3.5 ± 1.0	8.0 ± 1.0	15.5 ± 3.5
		1,526 ± 45 ($n = 10$)	4.5 ± 2.0	9.0 ± 2.0	23.0 ± 8.5
Figure 4b	0.88	163 ± 14 ($n = 5$)	2.0 ± 0.4	7.0 ± 1.0	15.0 ± 2.4
		420 ± 77 ($n = 5$)	2.1 ± 0.8	8.0 ± 2.0	14.6 ± 2.8

*The tomograms were generated from different cellular regions of thickness T. The measurements were obtained from line scans extracted from the tomograms across nanoparticles at different vertical heights (z). For horizontal (xy) line scans, two values are given: the 25–75% edge width ($r_{25–75}$) and the full-width at half-maximum (FWHM) measured from the smallest nanoparticles. In the vertical (xz) direction, only FWHM values are given. The error represents the standard deviation of n measurements made from 10 and 5 nanoparticles from tomograms corresponding to Figures 3b and 4b, respectively.

Inelastic Scattering and Sample Thickness

The energy loss distribution of the electrons that have been scattered inelastically in the specimen was measured using electron energy loss spectroscopy (EELS) from the location indicated by the rectangle in Figure 2a. The energy spectrum recorded from this region takes the form of a broad peak with a full-width at half-maximum (FWHM), ΔE of 248 eV, and a maximum energy loss at 185 eV. The FWHM of the energy distribution of the transmitted electrons can be calculated from the expression:

$$\Delta E = \frac{N_A e^4 Z \rho T}{2\pi\varepsilon_0 W m_0^2 v^2}, \quad (1)$$

where N_A is Avogadro's number, e the elementary charge, Z the atomic number, ρ the density, T the thickness of the specimen, ε_0 the permittivity of free space, W the atomic weight, m_0 the mass, and v the velocity of the electrons (Reimer & Kohl, 2008). As the local density of a critical point dried sample cannot be determined precisely, the present sample was considered to consist of amorphous carbon as an approximation. For $\Delta E = 248$ eV, equation (1) is then consistent with a specimen thickness of 2.4 μm. The thickness of the same region was also determined directly from the tomogram. The average specimen thickness at five equidistant locations within this region was measured to be 1.7 ± 0.3 μm, including the top membrane ruffles. The slight discrepancy between the value determined using EELS and that measured from the tomogram may result from the presence of osmium tetroxide, the silicon nitride support membrane, and the difference between the density of amorphous carbon and that of the actual cellular material carbon coating, which each contribute to the density of the specimen.

Resolving the Nanoparticles

Figure 3a shows a bright-field TEM image recorded from a perinuclear region, with the dashed line indicating the nucleus. In order to resolve individual nanoparticles, a tilt series of bright-field images was recorded at higher magnification from the region indicated by the square in Figure 3a. The 0° tilt image of the resulting tilt series is shown in Figure 3b. The darker region corresponds to the nucleus, while LDL-gold clusters and plasma membrane ruffles are also visible. Single nanoparticles can be seen, and the smaller and larger ones are distinguishable. The resulting tomogram was used to obtain a value for the total specimen thickness of this region of 2.09 μm (Supplementary Movie 4), measured from the lowest nanoparticle to the top plasma membrane ruffles. Clusters of LDL-gold nanoparticles were found to be distributed in a 1.67-μm-thick intracellular space, measured from the first cluster located in the lowest region of the cell to the highest cluster. A maximal intensity visualization of the tomogram, in which the vertical location of each cluster is color coded, is shown in Figure 3c.

Spatial Resolution

The achievable spatial resolution in the perinuclear region (Fig. 3b) was determined in both the horizontal and the vertical direction from line scans extracted from the tomogram across the smallest nanoparticles located either at the bottom, in the middle, or at the top of the cell. As a measure of the horizontal resolution, we used the 25–75% edge width ($r_{25–75}$) of the intensity peaks in line scans over the nanoparticles, which is a pessimistic measure of resolution for the case that the point spread function (PSF) is smaller than the object (Reimer & Kohl, 2008). The measurements show that the horizontal resolution varies between 2.5 nm for a particle located at the bottom of the cell and 4.5 nm for a particle located at the top, for a specimen thickness of 2.09 μm (see Table 1). The nanoparticle diameters were measured from the FWHM values, and were indeed much larger than the $r_{25–75}$ values, and thus the $r_{25–75}$ values serves as measure of the resolution. The highest resolution for TEM was obtained at the bottom of the sample with respect to a downward traveling electron beam. Both elastic scattering in the specimen and the fact that the particles are then further from focus are assumed to be responsible for the loss of resolution for nanoparticles that are higher in the sample.

In the vertical direction, the FWHM values were larger than the nanoparticle diameters and thus represent mea-

sures of the vertical resolution (with the PSF apparently larger than the nanoparticles in the vertical direction) (de Jonge et al., 2010*b*). The vertical resolution values increased from 16 to 23 nm on going from the bottom to the top of the specimen. The vertical resolution was lower than the horizontal resolution on account of the limited tilt range. The vertical elongation factor (e_{yz}) of the nanoparticles in the tomograms can be calculated using the Crowther Criterion, which determines the elongation of an object in the vertical direction due to the missing wedges in tomogram reconstructions (Radermacher, 1980):

$$e_{yz} = \sqrt{(\alpha + \sin(\alpha)\cos(\alpha))/(\alpha - \sin(\alpha)\cos(\alpha))}, \qquad (2)$$

where α is the maximal tilt angle in radians from 0°. For a specimen tilt range of 74°, e_{yz} is predicted to be 2.6, leading to an expected vertical elongation of 18 nm for a nanoparticle diameter of 7 nm. This value is consistent with the measurements to within experimental error for nanoparticles located at the bottom of the sample.

Clusters of LDL-Gold Nanoparticles

We also examined a thinner region of a cell at higher magnification, in order to study the constituents of individual clusters (Fig. 4a). The chosen region contained round electron-transparent cellular features, which are likely to be vesicles/vacuoles that are filled with lipid, a characteristic feature of macrophage foam cells. A first tomogram was reconstructed from a tilt series of images recorded at a magnification of 17,000× from the boxed region in Figure 4a (data not shown). The specimen thickness in this region was measured to be 0.88 μm from the bottom of the cell to the top membrane ruffles. In a second tilt series, which was centered on the same region but recorded at a higher magnification of 34,000×, both nanoparticle diameters of 7 and 16 nm can be distinguished (see arrows in Fig. 4b).

In this region, nanoparticles that are located at the top and bottom of the cellular volume both have horizontal spatial resolutions of 2 nm (see Table 1). The nanoparticles are again elongated in the vertical direction in a tomographic reconstruction computed from this region (Supplementary Movie 5), with lengths of 15 nm measured from the 34,000× magnification tilt series (Supplementary Movie 5). This value is consistent with the predicted vertical elongation determined from equation (2).

As the nanoparticles are spherical, have known diameters, and are separated from each other spatially, it was possible to determine their 3D positions with better precision than the vertical resolution of the tomogram. The positions of 813 nanoparticles with a diameter of 7 nm and 266 nanoparticles with a diameter of 16 nm were measured and incorporated into a 3D model of the cell (Fig. 4c; Supplementary Movie 5). By making use of the criterion that a cluster of nanoparticles contains at least ten nanoparticles, we found seven clusters in this region containing only small nanoparticles (with 58 ± 38 nanoparticles per cluster) and four clusters containing both small and large nanoparticles (with 92 ± 56 small and 67 ± 42 large nanoparticles per cluster). The two categories of nanoparticles, with different sizes representing successive days of loading, were observed to have assembled into separate clusters, several of which had then assembled together. This result suggests that cargo compartments, presumably lysosomes, combine over time with newly formed compartments to assemble into multivesicular bodies (Ikonen, 2008). Supplementary Movie 5 also shows that the smaller and larger nanoparticles do not mix, but merely assemble in adjacent clusters, each of which contains nanoparticles of different size. It could thus be speculated that the lysosomes combine without fusing their cargo (Baudoin et al., 2013).

Conclusions

Tilt series of bright-field images of a whole mount macrophage cell containing gold nanoparticles coated with LDL have been recorded using chromatic aberration-corrected TEM over a specimen tilt range of 74° in total. An important advantage of chromatic aberration correction is that regions of the specimen that have different thickness can all be imaged at an optimal defocus in the same field of view. For a cellular thickness of 0.88 μm, the spatial resolution of the recorded images was measured to be 2 nm for nanoparticles that are located through the thickness of the specimen, whereas the vertical elongation of the 3D image of a nanoparticle in the resulting tomogram amounted to 15 nm. For a cellular thickness of 2.09 μm, the horizontal resolution was measured to vary between 2.5 and 4.5 nm between particles located at the bottom and the top of the specimen, respectively. The difference in resolution is thought to result from a combination of elastic scattering in the specimen and blurring resulting from the significantly different defocus of different regions of the specimen. For the thicker region, the vertical elongation of 7-nm nanoparticles was measured to be between 15.5 and 23 nm for particles at the bottom and the top of the specimen, respectively. These values should be interpreted with caution, as they are specific to the present sample configuration, composition, and image acquisition parameters.

In the present study, the use of nanoparticles of known size and shape allowed the construction of a precise 3D model of nanoparticle locations from a tilt series of images acquired over a limited range of specimen tilt angles. Our results indicate that clusters of LDL-gold taken up on different days join into larger clusters without mixing their cargo. The ability to study whole cells in 3D on the nanometer scale provides new opportunities for quantitative studies of cell function with efficient use of electron dose, while avoiding artifacts introduced by sectioning. The efficient dose usage of chromatic aberration correction compared with energy-filtered TEM may benefit cryotomography of cells (Gan & Jensen, 2012) in future studies.

Acknowledgments

We thank B.K. Choi, B. Cox, M.L. Dawes, W.G. Jerome, and C.E. Romer for help with the experiments, D.W. Piston for discussions, and E. Arzt for support through the INM.

Electron microscopy was performed at the Ernst Ruska-Centre for Microscopy and Spectroscopy with Electrons, Forschungszentrum Jülich, Germany. This research was supported by NIH grant R01-GM081801.

References

Aoyama, K., Takagi, T., Hirase, A. & Miyazawa, A. (2008). STEM tomography for thick biological specimens. *Ultramicroscopy* **109**, 70–80.

Baudoin, J.P., Jerome, W.G., Kubel, C. & de Jonge, N. (2013). Whole-cell analysis of low-density lipoprotein uptake by macrophages using STEM tomography. *PLoS One* **8**, e55022.

de Jonge, N., Poirier-Demers, N., Demers, H., Peckys, D.B. & Drouin, D. (2010*a*). Nanometer-resolution electron microscopy through micrometers-thick water layers. *Ultramicroscopy* **110**, 1114–1119.

de Jonge, N., Sougrat, R., Northan, B.M. & Pennycook, S.J. (2010*b*). Three-dimensional scanning transmission electron microscopy of biological specimens. *Microsc Microanal* **16**, 54–63.

Dukes, M.J., Ramachandra, R., Baudoin, J.P., Jerome, W.G. & de Jonge, N. (2011). Three-dimensional locations of gold-labeled proteins in a whole mount eukaryotic cell obtained with 3 nm precision using aberration-corrected scanning transmission electron microscopy. *J Struct Biol* **174**, 552–562.

Engel, A. (2009). Scanning transmission electron microscopy: Biological applications. *Adv Imag Elect Phys* **159**, 357–386.

Frens, G. (1973). Controlled nucleation for regulation of particle-size in monodisperse gold suspensions. *Nature Phys Sci* **241**, 20–22.

Gan, L. & Jensen, G.J. (2012). Electron tomography of cells. *Q Rev Biophys* **45**, 27–56.

Gusnard, D. & Kirschner, R.H. (1977). Cell and organelle shrinkage during preparation for scanning electron microscopy: Effects of fixation, dehydration and critical point drying. *J Microsc* **110**, 51–57.

Haider, M., Hartel, P., Muller, H., Uhlemann, S. & Zach, J. (2009). Current and future aberration correctors for the improvement of resolution in electron microscopy. *Philos Transact A Math Phys Eng Sci* **367**, 3665–3682.

Heymann, J.A., Hayles, M., Gestmann, I., Giannuzzi, L.A., Lich, B. & Subramaniam, S. (2006). Site-specific 3D imaging of cells and tissues with a dual beam microscope. *J Struct Biol* **155**, 63–73.

Hoenger, A. & McIntosh, J.R. (2009). Probing the macromolecular organization of cells by electron tomography. *Curr Opin Cell Biol* **21**, 89–96.

Hohmann-Marriott, M.F., Sousa, A.A., Azari, A.A., Glushakova, S., Zhang, G., Zimmerberg, J. & Leapman, R.D. (2009). Nanoscale 3D cellular imaging by axial scanning transmission electron tomography. *Nat Methods* **6**, 729–731.

Hohn, K., Sailer, M., Wang, L., Lorenz, M., Schneider, M.E. & Walther, P. (2011). Preparation of cryofixed cells for improved 3D ultrastructure with scanning transmission electron tomography. *Histochem Cell Biol* **135**, 1–9.

Ikonen, E. (2008). Cellular cholesterol trafficking and compartmentalization. *Nat Rev Mol Cell Biol* **9**, 125–138.

Jerome, W.G., Cox, B.E., Griffin, E.E. & Ullery, J.C. (2008). Lysosomal cholesterol accumulation inhibits subsequent hydrolysis of lipoprotein cholesteryl ester. *Microsc Microanal* **14**, 138–149.

Jerome, W.G. & Yancey, P.G. (2003). The role of microscopy in understanding atherosclerotic lysosomal lipid metabolism. *Microsc Microanal* **9**, 54–67.

Kabius, B., Hartel, P., Haider, M., Muller, H., Uhlemann, S., Loebau, U., Zach, J. & Rose, H. (2009). First application of C_c-corrected imaging for high-resolution and energy-filtered TEM. *J Electron Microsc (Tokyo)* **58**, 147–155.

Koster, A.J., Grimm, R., Typke, D., Hegerl, R., Stoschek, A., Walz, J. & Baumeister, W. (1997). Perspectives of molecular and cellular electron tomography. *J Struct Biol* **120**, 276–308.

Kourkoutis, L.F., Plitzko, J.M. & Baumeister, W. (2012). Electron microscopy of biological materials at the nanometer scale. *Annu Rev Mater Res* **42**, 33–58.

Kremer, J.R., Mastronarde, D.N. & McIntosch, J.R. (1996). Computer visualization of three-dimensional image data using IMOD. *J Struct Biol* **116**, 71–76.

Larabell, C.A. & Nugent, K.A. (2010). Imaging cellular architecture with X-rays. *Curr Opin Struct Biol* **20**, 623–631.

Leary, R. & Brydson, R. (2011). Chromatic aberration correction: The next step on electron microscopy. *Adv Imag Elect Phys* **165**, 73–130.

Luzio, J.P., Pryor, P.R. & Bright, N.A. (2007). Lysosomes: Fusion and function. *Nat Rev Mol Cell Biol* **8**, 622–632.

Medalia, O., Weber, I., Frangakis, A.S., Nicastro, D., Gerisch, G. & Baumeister, W. (2002). Macromolecular architecture in eukaryotic cells visualized by cryoelectron tomography. *Science* **298**, 1209–1213.

Moore, K.J. & Tabas, I. (2011). Macrophages in the pathogenesis of atherosclerosis. *Cell* **145**, 341–355.

Pierson, J., Sani, M., Tomova, C., Godsave, S. & Peters, P.J. (2009). Toward visualization of nanomachines in their native cellular environment. *Histochem Cell Biol* **132**, 253–262.

Radermacher, M.H.W. (1980). Properties of three-dimensionally reconstructed objects from projections by conical tilting compared to single axis tilting. *Proc 7th Eur Congr Electron Microsc Den Haag* **1**, 132–133.

Reimer, L. & Gentsch, P. (1975). Superposition of chromatic error and beam broadening in transmission electron microscopy of thick carbon and organic specimens. *Ultramicroscopy* **1**, 1–5.

Reimer, L. & Kohl, H. (2008). *Transmission Electron Microscopy: Physics of Image Formation*. New York: Springer.

Reimer, L. & Ross-Messemer, M. (1987). Top-bottom effect in energy-selecting transmission electron microscopy. *Ultramicroscopy* **21**, 385–387.

Sousa, A.A., Aronova, M.A., Kim, Y.C., Dorward, L.M., Zhang, G. & Leapman, R.D. (2007). On the feasibility of visualizing ultrasmall gold labels in biological specimens by STEM tomography. *J Struct Biol* **159**, 507–522.

van Aert, S., Batenburg, K.J., Rossell, M.D., Erni, R. & van Tendeloo, G. (2011). Three-dimensional atomic imaging of crystalline nanoparticles. *Nature* **470**, 374–377.

Yakushevska, A.E., Lebbink, M.N., Geerts, W.J., Spek, L., van Donselaar, E.G., Jansen, K.A., Humbel, B.M., Post, J.A., Verkleij, A.J. & Koster, A.J. (2007). STEM tomography in cell biology. *J Struct Biol* **159**, 381–391.

Yancey, P.G., Miles, S., Schwegel, J. & Jerome, W.G. (2002). Uptake and trafficking of mildly oxidized LDL and acetylated LDL in THP-1 cells does not explain the differences in lysosomal metabolism of these two lipoproteins. *Microsc Microanal* **8**, 81–93.